Limit Analysis of Irregular Masonry with Rigid and Deformable Blocks

Yahroun Fei Long Hermans[1,2(✉)], Yiwei Hua[2], Karim Ehab Moustafa Kamel[1], Thierry Jacques Massart[1], and Gabriele Milani[2]

[1] Université libre de Bruxelles, Brussels 1050, Belgium
yahroun.fei.hermans@ulb.be
[2] Politecnico di Milano, Milan 20133, Italy

Abstract. The mechanical behavior of masonry assemblies is strongly influenced by the geometry and connectivity of the mortar joint network. While mesoscale modeling approaches are commonly developed for regular bond patterns, the analysis of irregular masonry systems remains comparatively less explored. In particular, the application of deformable element kinematic limit analysis to irregular masonry geometries has received limited attention. In this contribution, irregular masonry patterns are taken directly from an image of real irregular masonry. The geometry is subsequently processed into an interface-based description in which joints are lumped onto zero-thickness interfaces separating adjacent blocks. The resulting assemblies are analyzed using kinematic limit analysis. Both rigid and deformable block formulations are considered, allowing the influence of block deformability on the predicted structural response to be assessed. In the rigid formulation, energy dissipation is confined to the interfaces, whereas in the deformable formulation, dissipation occurs both at the interfaces and within the blocks through in-element plastic deformation. Interfaces between blocks are described using a Mohr–Coulomb failure criterion with a compression cap and tensile cut-off. Collapse loads are computed under combined loading conditions defined by biaxial unequal compression and biaxial unequal compression combined with shear. The resulting solutions provide insight into the collapse mechanisms and structural response of irregular masonry assemblies.

Keywords: Irregular Masonry · Engineering Homogenization · Kinematic Limit Analysis · Deformable Elements · Linear Programming · Second Order Cone Programming

1 Introduction

Masonry structures constitute a large portion of the existing building stock and remain widely used in construction practice. Their mechanical behavior is governed by the interaction between blocks and mortar joints, of which the

© The Author(s), under exclusive license to Springer Nature Switzerland AG 2027
O. Gervasi et al. (Eds.): ICCSA 2026 Workshops, LNCS 16758, pp. 515–532, 2027.
https://doi.org/10.1007/978-3-032-30497-1_31

arrangement strongly influences the global strength and failure mechanisms of the assembly [1–3]. Due to the presence of interfaces and the limited tensile strength of mortar joints, masonry typically exhibits a highly nonlinear and anisotropic mechanical response [4]. Consequently, the geometry and connectivity of the joint network play a fundamental role in determining the macroscopic behavior of masonry systems, particularly in the case of irregular masonry.

Various modeling approaches have been proposed to capture the mechanical behavior of masonry assemblies. At the structural scale, continuum models employing anisotropic constitutive laws are often used to describe the global response of masonry structures [5,6,22,23]. While computationally efficient, these approaches rely on phenomenological parameters that are not always directly linked to the underlying block–joint microstructure. To address this limitation, mesoscale modeling strategies explicitly represent the discrete nature of masonry by modeling blocks and mortar joints separately, allowing failure mechanisms to be described in terms of sliding and separation along interfaces [7]. In this context, joints are commonly represented as zero-thickness interfaces between adjacent blocks, providing an effective compromise between computational efficiency and an accurate representation of joint mechanics [8–10]. These approaches have proven particularly effective for analyzing collapse mechanisms and strength limits while retaining a clear connection to the underlying masonry topology [11,12].

Within the framework of limit analysis, alternative kinematic formulations have also been proposed, such as the Piecewise Rigid Displacement (PRD) method [24], which enables the automatic detection of collapse mechanisms based on dual energy criteria. More recently, limit analysis approaches have been extended toward engineering applications, including the seismic assessment of masonry façades [25]. In parallel, continuum approaches based on advanced constitutive modeling, such as multilaminate formulations [26], provide an alternative macroscopic description of masonry behavior.

However, many historical masonry structures exhibit strongly irregular block geometries and highly heterogeneous joint networks. Accurately capturing their behavior therefore requires modeling strategies capable of representing irregular masonry stackings. Several approaches have been proposed to generate masonry geometries for mechanical analysis. Image-based techniques allow the extraction of block geometries directly from photographs or scans of existing masonry assemblies, enabling realistic representations of irregular block arrangements [2,3]. Alternatively, synthetic geometry generation procedures may be used to construct masonry-like computational geometries with controlled morphological characteristics [13,14].

Limit analysis methods provide an efficient framework for investigating the collapse behavior of masonry systems [23]. In particular, kinematic limit analysis has been widely used to determine collapse mechanisms and failure envelopes of block assemblies interacting through frictional interfaces. In many formulations, masonry blocks are assumed to behave as rigid bodies, leading to efficient numerical procedures in which energy dissipation is concentrated exclusively at

the interfaces between blocks [2,3,10,15]. While this assumption is often justified by the relatively high stiffness of masonry units compared to mortar joints, it neglects the possibility of deformation and dissipation within the blocks themselves.

Recent developments have therefore introduced deformable element formulations of limit analysis [16], in which blocks are allowed to undergo internal deformation while still interacting through frictional interfaces. Unlike rigid-block formulations, where all energy dissipation is confined to interfaces, these approaches allow dissipation to occur both at the joints and within the blocks. This is achieved by constructing a suitable velocity interpolation and plastic constitutive behavior for the element, such that in-element plastic strains generate additional dissipation. Consequently, block deformability is not merely kinematic but also energetically active, contributing directly to the overall collapse mechanism and potentially influencing both failure modes and strength predictions.

Despite these developments, the role of block deformability in the limit analysis of masonry assemblies with complex geometries remains insufficiently understood. Most existing studies rely on idealized geometries or rigid-block formulations [2,3], and the combined effect of irregular block shapes and block deformability and dissipation on the predicted structural response has not been thoroughly investigated.

In this contribution, the limit analysis of irregular masonry assemblies is investigated using kinematic formulations. The geometrical input is directly taken from [18] and subsequently processed into two interface-based representations. The resulting geometries are analyzed using both rigid and deformable element kinematic limit analysis formulations. The influence of block deformability on the predicted collapse mechanisms and pressure is assessed under two loading conditions: (i) a combined compressive state defined by the loading direction $(\sigma_{xx}, \sigma_{yy}, \sigma_{xy}) = (-0.3\Gamma, -\Gamma, 0)$, and (ii) a combined compression-shear state defined by the loading direction $(\sigma_{xx}, \sigma_{yy}, \sigma_{xy}) = (-0.3\Gamma, -\Gamma, 0.6\Gamma)$ (as detailed in Sect. 4.2). By comparing rigid and deformable formulations on image-based masonry geometries, the present work aims to clarify the role of block deformability in the structural response of irregular masonry systems.

2 Lumped Joint Geometry Generation

The mechanical behavior of masonry assemblies is strongly influenced by the stacking arrangement of blocks. Accurately describing this geometry is therefore essential for reliable mechanical analysis. In the context of mesoscale modeling and the analysis of irregular masonry, however, constructing representative masonry geometries (RVEs) remains a challenging task. Existing approaches either rely on virtual generation techniques that aim to reproduce the morphological characteristics of masonry through synthetic procedures [13,14], or on image acquisition and segmentation methods, in which real or experimentally obtained geometries are transformed into computational models suitable for structural analysis [2,3,18]. In the present work, the point of departure is a RVE extracted from the bitmap data presented in [18].

2.1 Distance Field-Based Tessellation Procedure

The tessellation procedure relies on the computation of distance fields associated with the blocks. A distance field, denoted by DN_k, is defined over the entire RVE domain and represents the Euclidean distance from a point of the domain to the boundary of the k-th nearest block. As detailed in [2,3,13,14], the field DN_1 is defined as a signed distance field, taking positive values outside the inclusion and negative values inside.

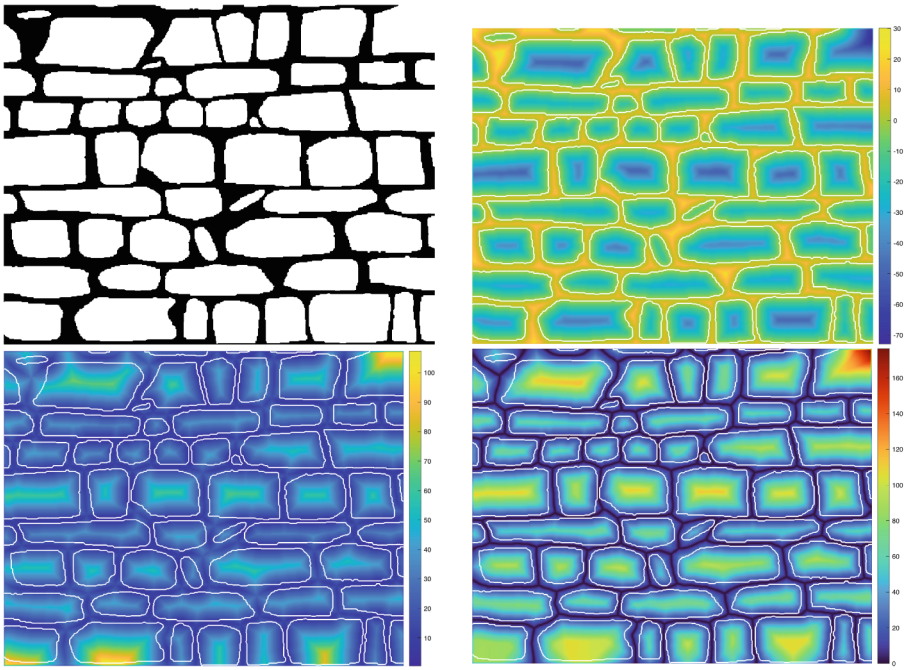


Fig. 1. Top left: Irregular masonry used in [18]. Top right: First nearest distance map. Bottom left: Second nearest distance map. Bottom right: The O_V function defined by Eq. (1). In the distance-based fields (top right and bottom subfigures), solid white lines indicate the block outlines.

The distance maps associated with the nearest neighboring blocks (Fig. 1) can be used to modify the spatial configuration of the block assembly. In particular, the distance functions DN_1 and DN_2, corresponding to the distances to the closest and second closest blocks at any point of the RVE, allow constructing a scalar field O_V the zero level set of which identifies the locus of points equidistant from these two blocks [13]:

$$O_V = DN_1(\mathbf{x}) - DN_2(\mathbf{x}) \tag{1}$$

This locus approximates the medial axis of the mortar joint network and therefore naturally delineates the boundaries between adjacent blocks, effectively lumping the joint.

For the kinematic limit analysis procedure, the scalar field O_V must be converted into a discrete representation of the mortar joint network composed of vertices and edges.

The adopted extraction procedure is based on the medial axis of the assembly. In the present context, only the outer medial axis is required, as it corresponds to the mortar joints separating adjacent blocks. The extraction is carried out in two stages, as defined in [2]: (i) The triple junctions are identified. These junctions are connected, and (ii) progressively refined to follow the zero-level of the O_V.

Let (k, l, m) denote three neighboring blocks. For each pair of blocks, a pairwise Voronoi-like function is introduced as

$$O_{V_{ij}}(\mathbf{x}) = DN_i(\mathbf{x}) - DN_j(\mathbf{x}), \qquad (i,j) \in \{(k,l),(l,m),(k,m)\}, \tag{2}$$

so that the triple junction $\mathbf{x}^*$ is defined by the simultaneous conditions

$$O_{V_{kl}}(\mathbf{x}^*) = 0, \qquad O_{V_{lm}}(\mathbf{x}^*) = 0, \qquad O_{V_{km}}(\mathbf{x}^*) = 0. \tag{3}$$

As described in [3], starting from an initial guess located in the vicinity of the junction, the point is iteratively displaced using the values of the functions $O_{V_{ij}}$ and their gradients $\nabla O_{V_{ij}}$ until the conditions in Eq. (3) are satisfied within a prescribed tolerance.

Once the triple junctions have been determined, neighboring junctions are connected using straight segments, yielding a simplified polygonal representation of the mortar joint network. This representation already provides a lumped geometry suitable for mechanical analysis. In a second stage, additional points are introduced along these segments and displaced toward the zero level sets of the corresponding pairwise functions $O_{V_{ij}}$. Repeating this procedure recursively yields a refined curved representation of the medial axis.

Algorithm (1) therefore provides two distinct geometric representations. The first one, $\mathcal{G}^{\text{simp}}$, is obtained by directly connecting the identified triple junctions and corresponds to a simplified straight-segment approximation of the mortar joint network. The second one, $\mathcal{G}^{\text{curv}}$, is obtained after recursive insertion and projection of intermediate edge points, resulting in a curved representation that follows the medial axis more closely. In both cases (Fig. 2), the extracted joint network is used to define the interface geometry required by the limit analysis formulation.

3 Kinematic Limit Analysis

The mechanical response of the masonry assemblies is analyzed using kinematic limit analysis. According to the kinematic theorem of limit analysis, collapse occurs when the external work associated with a kinematically admissible velocity field is equal to the internal energy dissipation within the system.

Algorithm 1: Extraction of simplified and curved lumped geometries

Input: Pairwise functions $O_{V_{ij}}(\mathbf{x})$; gradients $\nabla O_{V_{ij}}(\mathbf{x})$; tolerances ε and $\ell_{\max}$
Output: Simplified geometry $\mathcal{G}^{\text{simp}}$; Curved geometry $\mathcal{G}^{\text{curv}}$
$\mathcal{T} \leftarrow \emptyset$;
foreach *triplet of neighboring blocks* (k, l, m) **do**
  Choose an initial point $\mathbf{x}_0$ near the junction;
  $n \leftarrow 0$;
  while $\max\left(|O_{V_{kl}}(\mathbf{x}_n)|, |O_{V_{lm}}(\mathbf{x}_n)|, |O_{V_{km}}(\mathbf{x}_n)|\right) > \varepsilon$ **do**
    $\mathbf{x}_{n+1} = \mathbf{x}_n -$
    $\alpha \left(O_{V_{kl}}(\mathbf{x}_n)\nabla O_{V_{kl}}(\mathbf{x}_n) + O_{V_{lm}}(\mathbf{x}_n)\nabla O_{V_{lm}}(\mathbf{x}_n) + O_{V_{km}}(\mathbf{x}_n)\nabla O_{V_{km}}(\mathbf{x}_n)\right)$;
    $n \leftarrow n + 1$;
  $\mathcal{T} \leftarrow \mathcal{T} \cup \{\mathbf{x}_n\}$;
$\mathcal{G}^{\text{simp}} \leftarrow$ connect neighboring points of $\mathcal{T}$ with straight segments;
$\mathcal{G}^{\text{curv}} \leftarrow \mathcal{G}^{\text{simp}}$;
foreach *edge* e *in* $\mathcal{G}^{\text{curv}}$ **do**
  while *segment length* $> \ell_{\max}$ **do**
    insert midpoint $\mathbf{p}$ on segment;
    find neighboring blocks (i, j) of $\mathbf{p}$;
    while $|O_{V_{ij}}(\mathbf{p})| > \varepsilon$ **do**
      $\mathbf{p} \leftarrow \mathbf{p} - \dfrac{O_{V_{ij}}(\mathbf{p})}{\|\nabla O_{V_{ij}}(\mathbf{p})\|^2} \nabla O_{V_{ij}}(\mathbf{p})$;
return $\mathcal{G}^{\text{simp}}, \mathcal{G}^{\text{curv}}$;

In rigid block formulations, energy dissipation is exclusively concentrated at the interfaces, as the blocks are assumed to remain undeformed. In contrast, when block deformability is introduced, an additional dissipation mechanism can be activated within the blocks through the assignment of a continuum-type constitutive behavior, allowing in-element plastic deformation to contribute directly to the total dissipation alongside the interfacial contribution. In this work, both formulations are considered: (i) the rigid block formulation and (ii) the deformable/dissipating block formulation.

3.1 Rigid Block Formulation

As discussed in [3], masonry units are assumed in this case to behave both as infinitely stiff and infinitely strong in the rigid block formulation. Consequently, deformation and failure cannot occur within the blocks themselves and are confined to the interfaces separating adjacent blocks, corresponding to the mortar joints. Relative normal and tangential displacements may therefore develop only along these interfaces.

The mechanical behavior of the joints is described using a perfect rigidplastic constitutive model governed by a yield criterion. According to the classical assumptions of limit analysis [11], plastic flow follows an associated flow rule. In

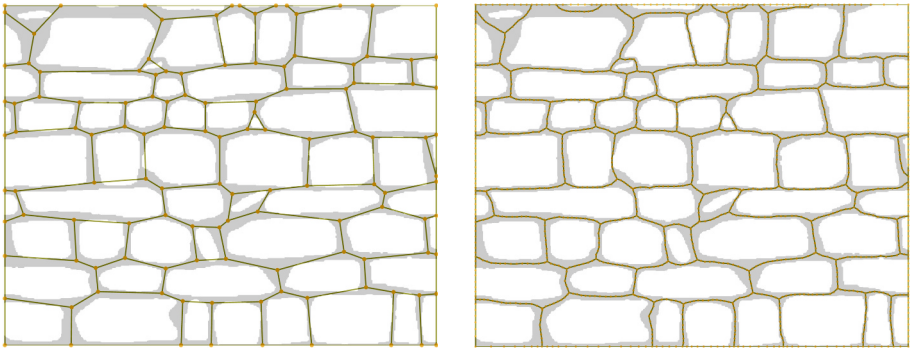


Fig. 2. Left: Geometry after lumping joints resulting from connecting triple junctions. Right: Lumped joint geometry after further joint delineation.

the present formulation, interface failure is governed by a Mohr–Coulomb criterion with compression cap and tensile cut-off (see [21] for more details), hereafter referred to as the modified Mohr–Coulomb criterion. Furthermore, small displacement rates are assumed, allowing the block kinematics to be linearized.

Under these assumptions, collapse mechanisms are described by discontinuous velocity fields characterized by relative velocity jumps across the interfaces. The corresponding collapse load is obtained by enforcing the Principle of Virtual Powers, which equates the external work of the applied loads to the internal rate of dissipation along the interfaces.

Constitutive Equations. The velocity jump across an interface, expressed in the local reference frame, follows the associated flow rule:

$$\Delta\tilde{\dot{\mathbf{u}}} = \dot{\boldsymbol{\lambda}}\frac{\partial f(\boldsymbol{\sigma})}{\partial \boldsymbol{\sigma}} \tag{4}$$

where $f(\boldsymbol{\sigma})$ denotes the yield surface, here defined by a modified Mohr–Coulomb criterion, and $\dot{\boldsymbol{\lambda}}$ represents the non-negative plastic multiplier rates.

To solve the problem as a linear programming problem, the yield surface is linearized. Equation (4) can therefore be expressed as

$$\dot{\boldsymbol{\lambda}}\frac{\partial f(\boldsymbol{\sigma})}{\partial \boldsymbol{\sigma}} = \sum_{e=1}^{N_p} \dot{\lambda}_e \frac{\partial f(\boldsymbol{\sigma})_e}{\partial \boldsymbol{\sigma}} \tag{5}$$

where N_p denotes the number of branches used to approximate the linearized failure criterion. The plastic multipliers satisfy the standard Kuhn-Tucker conditions [17].

The velocity jump expressed in the local coordinate system is related to the global reference frame through the rotation matrix $\mathbf{R}$:

$$\Delta\tilde{\dot{\mathbf{u}}} = \mathbf{R}\Delta\dot{\mathbf{u}} \tag{6}$$

Due to the rigid-block assumption and small displacement rates, the velocity of any point P belonging to a block with centroid G can be written as

$$\dot{\mathbf{u}}_P = \mathbf{A}_G^P \dot{\mathbf{x}}_{k,j}, \qquad \mathbf{A}_G^P = \begin{bmatrix} 1 & 0 & -(y^P - y^G) \\ 0 & 1 & (x^P - x^G) \end{bmatrix} \tag{7}$$

where $\mathbf{A}_G^P$ is the kinematic matrix and $\dot{\mathbf{x}}_{k,j}$ is the vector of degrees of freedom associated with the centroid of the jth block. Under the rigid-body assumption, the block kinematics are defined by two translational and one rotational velocity:

$$\dot{\mathbf{x}}_{k,j} = \left[\dot{u}_x,\ \dot{u}_y,\ \dot{\phi}_z\right]^\top, \qquad j = 1, \ldots, N_B \tag{8}$$

where N_B denotes the number of blocks in the assembly.

Combining Eqs. (6) and (7), the velocity jump at a discretization point P_i located on the interface between blocks j and $j+1$ can be expressed as

$$\Delta\tilde{\dot{\mathbf{u}}}_{P_i} = \mathbf{R}\left(\mathbf{A}_{G,j+1}^{P_i}\dot{\mathbf{x}}_{k,j+1} - \mathbf{A}_{G,j}^{P_i}\dot{\mathbf{x}}_{k,j}\right) \tag{9}$$

Substituting Eq. (5) and (9) into Eq. (4) yields the compatibility condition for a discretized interface point:

$$\mathbf{R}\left(\mathbf{A}_{G,j+1}^{P_i}\dot{\mathbf{x}}_{k,j+1} - \mathbf{A}_{G,j}^{P_i}\dot{\mathbf{x}}_{k,j}\right) - \sum_{e=1}^{N_p} \dot{\lambda}_e \frac{\partial f(\boldsymbol{\sigma})_e}{\partial \boldsymbol{\sigma}} = 0 \tag{10}$$

Virtual Power. Since dissipation occurs only along the interfaces, the collapse load multiplier Γ is obtained by enforcing the Principle of Virtual Powers:

$$\Gamma P_{ext,unit} = P_{in} \qquad \Longleftrightarrow \qquad \Gamma = \frac{P_{in}}{P_{ext,unit}} = \frac{\mathbf{c}^\top \mathbf{x}}{P_{ext,unit}} \tag{11}$$

where P_{in} denotes the internal dissipation power and $P_{ext,unit}$ the externally applied unit load. The vector $\mathbf{c}$ collects the coefficients such that $P_{in} = \mathbf{c}^\top \mathbf{x}$. The vector of unknowns is defined as

$$\mathbf{x} = \left[\dot{\mathbf{x}}_k, \dot{\boldsymbol{\lambda}}\right],$$

which gathers the kinematic variables and the plastic multiplier rates.

Canonical Form. The resulting problem can be formulated as a linear programming minimization problem:

$$\begin{aligned} &\text{minimize} \quad \Gamma = \mathbf{c}^\top \mathbf{x} \\ &\text{subject to } \mathbf{A}^* \mathbf{x} = \mathbf{b} \\ &\qquad\qquad \dot{\boldsymbol{\lambda}} \geq \mathbf{0} \end{aligned} \tag{12}$$

where $\mathbf{A}^*$ and $\mathbf{b}$ define the equality constraints resulting from the constitutive relations and the normalization of the externally applied power.

3.2 Deformable Polygon Blocks

Starting from the rigid block formulation presented in Sect. 3.1, the extension to deformable polygonal elements requires only minor modifications. This follows directly from the interface-based framework, where interfacial discontinuities are already explicitly represented.

From a kinematic standpoint, the main modification consists in enriching the matrix $\mathbf{A}_G^P$ used to describe the velocity field within each element. In addition to rigid body motion, three additional modes are introduced to account for constant-strain deformation within the polygonal elements, corresponding to axial deformation in the x- and y-directions and in-plane xy shear.

Accordingly, the vector of unknowns $\dot{\mathbf{x}}_k$ associated with each block j is extended to include three additional degrees of freedom, representing the constant strain-rate components $\dot{\varepsilon}_x$, $\dot{\varepsilon}_y$, and $\dot{\varepsilon}_{xy}$. The resulting kinematic description is expressed as

$$\begin{aligned} \mathbf{A}_G^P &= \begin{bmatrix} 1 & 0 & -(y^P - y^G) & (x^P - x^G) & 0 & (y^P - y^G) \\ 0 & 1 & (x^P - x^G) & 0 & (y^P - y^G) & (x^P - x^G) \end{bmatrix} \\ \dot{\mathbf{x}}_{k,j} &= \begin{bmatrix} \dot{u}_x, & \dot{u}_y, & \dot{\phi}_z, & \dot{\varepsilon}_x, & \dot{\varepsilon}_y, & \dot{\varepsilon}_{xy} \end{bmatrix}^\top \end{aligned} \tag{13}$$

Substituting this enriched kinematic operator into the formulation, the velocity jumps at the interfaces can be computed in a manner consistent with the rigid block case (Eq. (9)).

The introduction of element deformation requires a constitutive model to constrain the additional strain-rate variables. Here, a continuum plasticity model is adopted, combining a Mohr–Coulomb criterion (Eq. (14)) with a compression cap defined in principal stress space (Eq. (15)). Both criteria can be expressed in a conic quadratic form, allowing their incorporation into a convex optimization framework.

$$F_{\mathrm{MC}}(\boldsymbol{\sigma}) = (\sigma_x - \sigma_y)^2 + (2\tau_{xy})^2 - (2c\cos\varphi - (\sigma_x + \sigma_y)\sin\varphi)^2 \tag{14}$$

$$F_{\mathrm{C}}(\boldsymbol{\sigma}) = (\sigma_x - \sigma_y)^2 + (2\tau_{xy})^2 - (2\sigma_c + (\sigma_x + \sigma_y))^2 \tag{15}$$

Within the kinematic formulation, plastic flow is governed by an associated flow rule. For each conic surface, three plastic multipliers are introduced to describe the corresponding plastic flow. As a consequence of associativity, these multipliers are constrained to lie within the second-order cones that are dual to the constitutive one. The compatibility condition for the deformable elements can thus be written as:

$$\begin{aligned} \mathbf{B}_j \dot{\mathbf{x}}_{k,j} &= \sum_{e=1}^{3} \dot{\lambda}_e^{\mathrm{MC}} \frac{\partial F_{\mathrm{MC}}(\boldsymbol{\sigma})_e}{\partial \boldsymbol{\sigma}} + \sum_{e=1}^{3} \dot{\lambda}_e^{\mathrm{C}} \frac{\partial F_{\mathrm{C}}(\boldsymbol{\sigma})_e}{\partial \boldsymbol{\sigma}} \\ \mathbf{B}_j &= [\mathbf{O}_{3\times 3}\ \mathbf{I}_{3\times 3}], \quad \dot{\lambda}_e^{\mathrm{MC}}, \dot{\lambda}_e^{\mathrm{C}} \in \mathcal{Q}^3 := \{\mathbf{x} : x_1 \geq \|(x_2, x_3)\|_2\} \end{aligned} \tag{16}$$

where the matrix $\mathbf{B}_j$ extracts the deformation-related components from the global vector of unknowns [16].

As a result of these modifications, the kinematic limit analysis problem for deformable elements can be formulated as a Second-Order Cone Programming (SOCP) problem:

$$\begin{aligned} &\text{minimise} \quad \Gamma = \mathbf{c}^\top \mathbf{x} \\ &\text{subject to} \quad \mathbf{A}^* \mathbf{x} = \mathbf{b} \\ &\qquad\qquad \dot{\boldsymbol{\lambda}} \geq \mathbf{0},\ \dot{\boldsymbol{\lambda}}_1 \in \mathcal{Q}_1^3 \times \mathcal{Q}_2^3 \times \cdots \times \mathcal{Q}_l^3 \end{aligned} \tag{17}$$

where l refers to the number of non-interface (deformable) elements, and $\mathcal{Q}^3$ denotes a three-dimensional second-order cone. For each element, three plastic multiplier components are introduced, corresponding to the adopted yield criteria (Mohr–Coulomb, compression cap, and tensile cut-off).

Compared to the rigid block formulation, additional constraints associated with the element deformation (Eq. (16)) must be introduced, and the vector of unknowns is extended as

$$\mathbf{x} = \left[\dot{\mathbf{x}}_k, \dot{\boldsymbol{\lambda}}, \dot{\boldsymbol{\lambda}}_1\right],$$

where $\dot{\boldsymbol{\lambda}}_1$ denotes the plastic multipliers associated with the in-element constitutive model (i.e. $\dot{\lambda}_e^{\mathrm{C}}$ or $\dot{\lambda}_e^{\mathrm{MC}}$ depending on the active criterion in the block).

In contrast to the rigid case, energy dissipation now arises both from interfacial mechanisms and from plastic deformation within the elements. The corresponding dissipation is incorporated into the objective function, which retains the form $\mathbf{c}^\top \mathbf{x}$. A detailed derivation of the formulation can be found in [16].

4 Results and Discussions

The kinematic limit analysis framework is used to investigate the mechanical response of the RVEs considered in Sect. 2. The aim is to assess the influence of block deformability by comparing the predictions from the rigid and deformable formulations.

The differences are expected to be more pronounced under compressive loading. Two loading scenarios are therefore considered: (i) biaxial compression and (ii) biaxial compression combined with shear. Both $\mathcal{G}^{\mathrm{curv}}$ and $\mathcal{G}^{\mathrm{simp}}$ are analyzed, allowing the combined effects of geometry and block deformability to be evaluated.

4.1 Representative Volume Element

The RVE has fixed dimensions of 869 mm in width and 684 mm in height (Fig. 3). As described in Sec. (2), two geometric representations are considered: (i) the curved geometry $\mathcal{G}^{\mathrm{curv}}$ and simplified geometry $\mathcal{G}^{\mathrm{simp}}$ respectively.

Based on the rigid and deformable element formulations, two modeling approaches are considered for the RVE: (i) the inclusions are treated as rigid

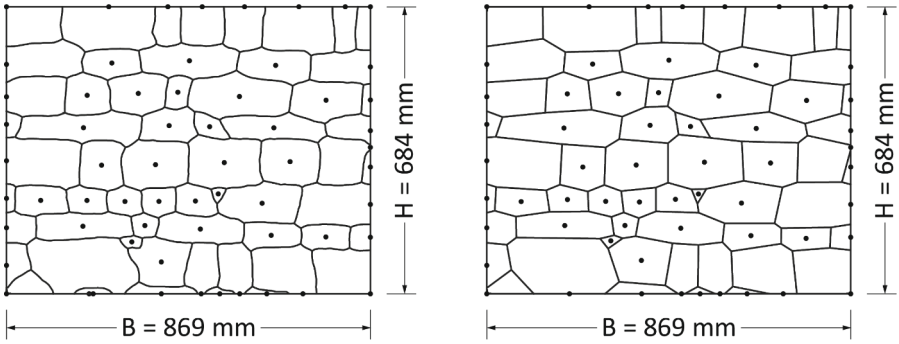


Fig. 3. Left: Curved interface-based geometry $\mathcal{G}^{\text{curv}}$ considered in the analysis. Right: Simplified interface-based geometry $\mathcal{G}^{\text{simp}}$ considered in the analysis.

blocks, and all dissipation is confined to the interfaces. Interface behavior is governed by a Mohr–Coulomb criterion supplemented with a compression cap and tensile cut-off to account for crushing and tensile failure; (ii) block deformability is introduced, allowing plastic deformation to develop within the polygonal inclusions. In this last case, in-element plasticity is described by a Mohr–Coulomb criterion combined with a compression cap.

Table 1. Material properties assumed for the interfaces and inclusions.

Interface		Element	
Cohesion	c	Cohesion	$5c$
Compression strength	$40c$	Compression strength	$40c$
Tension cutoff	$c/1.4$		

The interfacial cohesion is set to 50 kPa. The remaining strength parameters for both interfaces and inclusions are defined proportionally to this value for comparison purposes (Table 1). The friction angle φ is taken equal to 22° for both interfaces and elements, in accordance with the design code Italian Annex [19]. The slope of the compression cap for the interfaces is set to 45°.

The material parameters reported in Table 1 are selected to provide a consistent and controlled comparison between the rigid and deformable formulations. In particular, the interfacial cohesion is taken as a reference value, and the remaining strength parameters are defined proportionally in order to preserve realistic strength ratios between mortar joints and masonry units. The higher cohesion assigned to the elements reflects the typical mechanical contrast between blocks and mortar, where units exhibit significantly larger compressive and shear strength. The compression cap is introduced to account for crushing under high compressive stress states, which is particularly relevant under the

loading conditions considered. These assumptions are not intended to represent a specific material but rather to provide a representative parameter set suitable for comparative analysis.

4.2 Loads and Boundary Conditions

For each boundary, an additional node is introduced to impose a multi-point constraint (MPC) on the velocities of the boundary nodes (Fig. 4a). The four boundary segments of the RVE are denoted by $i \in \{\partial X^-, \partial X^+, \partial Y^-, \partial Y^+\}$, corresponding to the left, right, bottom, and top boundaries, respectively. Each of these nodes possesses two degrees of freedom in the global Cartesian system, associated with the averaged boundary velocities U_x^i and U_y^i in the corresponding directions (Eq. (18)).

For a given boundary segment i, the index $j \in i$ refers to the set of boundary edges belonging to that segment. Each edge j is defined by its end nodes A and B, with associated nodal velocities $u_x^{j,A}$, $u_x^{j,B}$ (and similarly for u_y), and length l_j. The averaged boundary velocities U_x^i and U_y^i are computed as weighted averages over these edges.

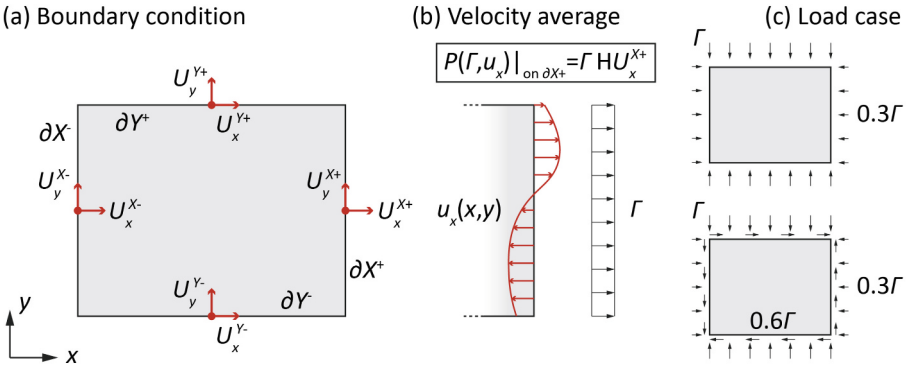


Fig. 4. Loading and boundary condition considered for RVE.

This formulation enforces an average boundary velocity based on the Principle of Virtual Work. The work of a uniform stress field acting on the boundary velocity distribution is taken to be equivalent to the work of the corresponding resultant acting on the MPC node (see Fig. 4b). The MPC conditions for the four boundaries can thus be expressed in matrix form as Eq. (19), where $\bar{\mathbf{U}}$ collects the averaged boundary velocities, and $\mathbf{L}_u$ is the matrix relating the global

velocity vector $\dot{\mathbf{x}}$ to these averaged quantities.

$$\begin{aligned} U_x^i &= \frac{1}{2}\frac{\sum_{j\in i}\left(u_x^{j,A}+u_x^{j,B}\right)l_j}{\sum l_j} \\ U_y^i &= \frac{1}{2}\frac{\sum_{j\in i}\left(u_y^{j,A}+u_y^{j,B}\right)l_j}{\sum l_j} \end{aligned}, \quad i=\partial X^-,\partial X^+,\partial Y^-,\partial Y^+ \tag{18}$$

$$\mathbf{L}_u\dot{\mathbf{x}}=\bar{\mathbf{U}}, \quad \bar{\mathbf{U}}=\left[U_x^{X^-}\ U_y^{X^-}\ \cdots U_x^{Y^+}\ U_y^{Y^+}\right]^\top \tag{19}$$

The biaxial compression case (Case A) is defined by Eq. (20), with the compression predominantly applied in the vertical direction. In the compression-shear case (Case B), an additional shear component is superimposed onto the same biaxial compression state (Fig. 4c).

The prescribed uniform stress field is applied along each boundary by computing the corresponding resultant force and assigning it to the associated MPC node. The corresponding external power can therefore be expressed in terms of the averaged boundary velocities (Eq. (21)), where the vector $\mathbf{q}$ collects the resultant forces associated with the prescribed stress field acting on each boundary segment.

Following the positive work condition [20], the external work is normalized to unity, such that the internal dissipation is directly equal to the collapse multiplier Γ.

$$\begin{aligned} &\text{Case A}: \sigma_{xx}=-0.3\Gamma,\ \sigma_{yy}=-\Gamma,\ \sigma_{xy}=0 \\ &\text{Case B}: \sigma_{xx}=-0.3\Gamma,\ \sigma_{yy}=-\Gamma,\ \sigma_{xy}=0.6\Gamma \end{aligned} \tag{20}$$

$$P_{ext,unit}=\mathbf{q}^\top\bar{\mathbf{U}}=1 \tag{21}$$

Including boundary MPC velocities also allows a convenient suppression of rigid body motion. To avoid rigid body translation, the averaged velocities on opposite boundaries are constrained to sum to zero (Eq. (22)). In addition, the averaged rotational rate of the RVE is enforced to be zero to suppress rigid body rotation (Eq. (23)). Using Green's theorem, this rotational term can be computed from the integral of the boundary velocity field, and is ultimately expressed as a linear combination of the MPC velocities. The periodic boundary conditions can thus be written in matrix form as Eq. (24), where Ω denotes the RVE domain, with area $|\Omega|$, width B, and height H.

Finally, the rotational rate of the boundary elements is constrained to zero in order to further reduce zero-dissipation deformation modes.

$$\begin{aligned} U_x^{X^+}+U_x^{X^-}&=0, \quad U_x^{Y^+}+U_x^{Y^-}=0 \\ U_y^{X^+}+U_y^{X^-}&=0, \quad U_y^{Y^+}+U_y^{Y^-}=0 \end{aligned} \tag{22}$$

$$\begin{aligned} \bar{W} :&= \frac{1}{2\,|\Omega|}\int_\Omega\left(\frac{\partial u_y}{\partial x}-\frac{\partial u_x}{\partial y}\right)\mathrm{d}\Omega=\frac{1}{2\,|\Omega|}\oint_{\partial\Omega}u_x\mathrm{d}y+u_y\mathrm{d}x \\ &= \frac{H}{|\Omega|}\left(U_y^{X^+}-U_y^{X^-}\right)+\frac{B}{|\Omega|}\left(U_x^{Y^+}-U_x^{Y^-}\right)=0 \end{aligned} \tag{23}$$

$$\mathbf{L}_m \bar{\mathbf{U}} = \mathbf{0} \tag{24}$$

where $\mathbf{L}_m$ is there constraint matrix for the periodic boundary conditions. All the aforementioned load and boundary conditions are incorporated into the equality constraints of the problem, i.e., within the matrix $\mathbf{A}^*$ and vector $\mathbf{b}$. The canonical formulations for the rigid and deformable cases remain unchanged (Eqs. (12) and (17)).

In the following, the collapse results obtained for both $\mathcal{G}^{\text{simp}}$ and $\mathcal{G}^{\text{curv}}$, under different element modeling assumptions, are presented. The computed collapse stresses are normalized with respect to the interfacial cohesion c.

5 Results

5.1 Collapse Results

Under biaxial compression, the use of rigid and deformable elements leads to different collapse mechanisms. In the rigid formulation, the macroscopic deformation is accommodated through interfacial mechanisms. The compressive response is characterized by the formation of extended horizontal crushing bands, accompanied by localized sliding along adjacent vertical joints (Fig. 5). Energy dissipation is therefore concentrated along interfaces aligned with the dominant stress direction. Boundary units, particularly smaller blocks, show pronounced relative motion, resulting in significant interface penetration. Failure of vertical joints is more pronounced for $\mathcal{G}^{\text{curv}}$ than for $\mathcal{G}^{\text{simp}}$, likely due to increased interlocking effects attributed to the geometrical roughness.

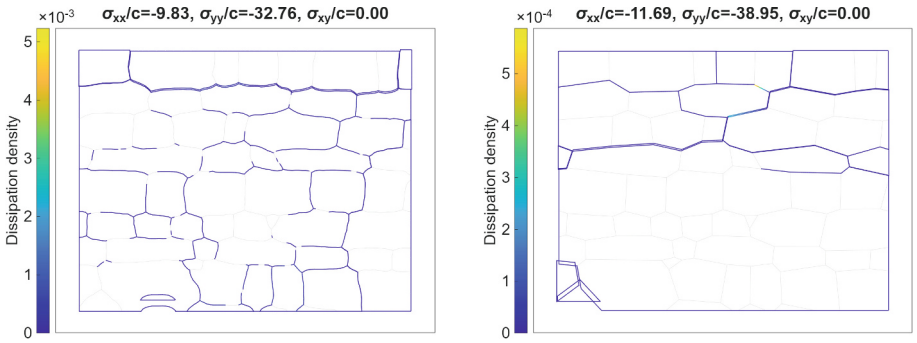


Fig. 5. Collapse mechanism of RVE under biaxial compression load, rigid units; left: $\mathcal{G}^{\text{curv}}$ - right: $\mathcal{G}^{\text{simp}}$.

In contrast, in the deformable formulation, the predicted deformation field is nearly uniform for both $\mathcal{G}^{\text{curv}}$ and $\mathcal{G}^{\text{simp}}$ (Fig. 6), with only minor localization observed in small boundary units. In this case, dissipation is no longer confined

to the interfaces but develops within the block interiors, leading to a more distributed deformation pattern. The resulting stress magnitude in the dominant compression direction is consistent with the prescribed compressive strength of the blocks.

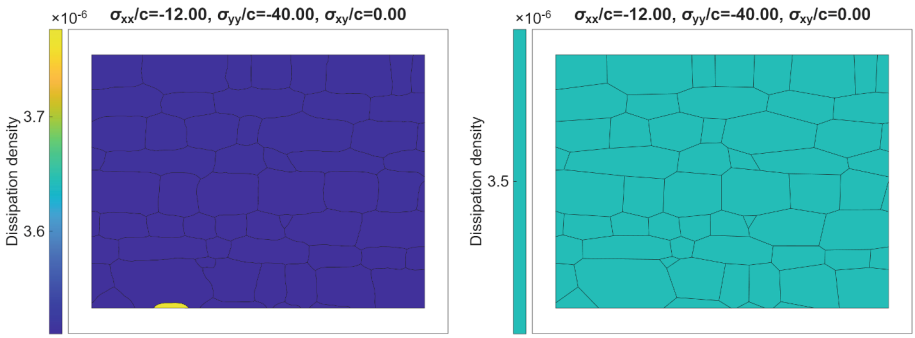


Fig. 6. Collapse mechanism of RVE under biaxial compression load, deformable units; left: $\mathcal{G}^{\text{curv}}$ - right: $\mathcal{G}^{\text{simp}}$.

The superimposed shear stress significantly alters the collapse behavior. The combined loading induces tensile effects along the diagonal of the RVE, partially counteracting the compressive state. As a result, in the rigid formulation, the horizontal crushing bands disappear and are replaced by pronounced interfacial separation and sliding (Fig. 7). Crushing is limited and primarily observed near boundary regions. Due to geometric interlocking, large portions of $\mathcal{G}^{\text{curv}}$ exhibit limited interfacial activity, resulting in a slightly higher collapse load compared to $\mathcal{G}^{\text{simp}}$.

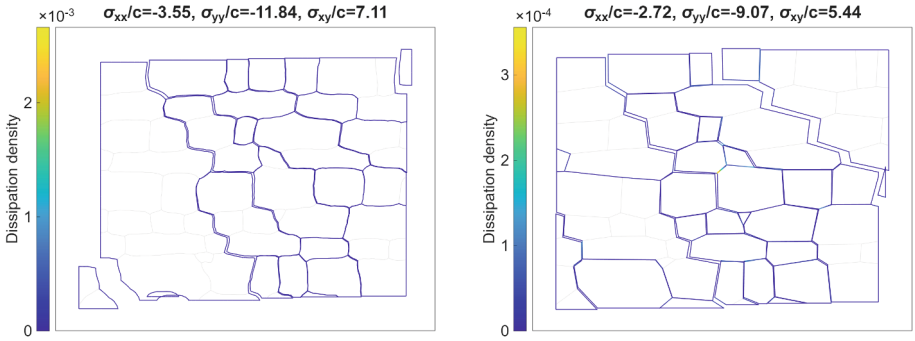


Fig. 7. Collapse mechanism of RVE under biaxial compression with shear, rigid units; left: $\mathcal{G}^{\text{curv}}$ - right: $\mathcal{G}^{\text{simp}}$.

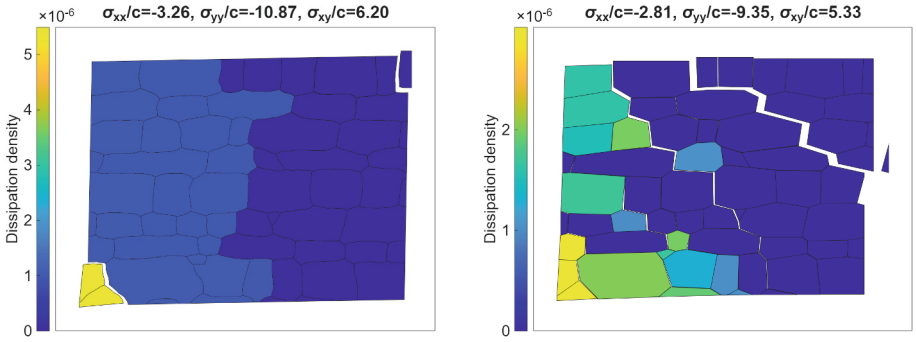


Fig. 8. Collapse mechanism of RVE under biaxial compression with shear, deformable units; left: $\mathcal{G}^{\text{curv}}$ - right: $\mathcal{G}^{\text{simp}}$.

A similar trend is observed in the results of the deformable formulation (Fig. 8). In $\mathcal{G}^{\text{curv}}$, the deformation field remains relatively continuous, reflecting a typical shear-dominated response, with dissipation concentrated in regions influenced by interlocking. In contrast, $\mathcal{G}^{\text{simp}}$ exhibits more pronounced interfacial separation, particularly near the boundaries, leading to a reduction in the predicted collapse load. Compared to the rigid-unit predictions, localized interfacial cracking is partially replaced by distributed in-element dissipation, resulting in a smearing of the failure pattern. Despite these differences, the locations of large cracks remain consistent between rigid and deformable formulations.

Overall, under combined compression-shear loading, the differences between rigid and deformable formulations are less pronounced. Both approaches provide consistent predictions in terms of collapse mechanisms and load levels.

5.2 Discussions

Despite the advantages of employing deformable elements, certain theoretical limitations must be acknowledged. In particular, constant-strain polygonal elements are prone to an internal locking phenomenon, as discussed in [16]. This issue arises from the constant-strain assumption, which is insufficient to fully represent the kinematics of polygonal blocks. As a result, additional constraints are introduced at the block level, leading to an overestimation of the collapse load. Several strategies may be adopted to alleviate this issue, including the use of piecewise-constant elements or the subdivision of polygonal blocks into triangular elements. The severity of the locking effect is expected to increase in the presence of high deformation gradients. However, in the context of RVE analysis under uniform stress fields, this effect is likely to remain limited, although this assumption requires further verification through dedicated comparative studies.

The present results nevertheless highlight the importance of accounting for block deformability when predicting the mechanical response of RVEs. Although the material parameters considered in this study are selected for comparative

purposes, the proposed framework allows the use of experimentally calibrated properties for realistic material characterization.

Furthermore, the proposed formulation can be extended to construct the homogenized failure surface of RVEs through an iterative procedure, which will be investigated in future work.

Acknowledgments. The first author gratefully acknowledges the support of the Fonds de la Recherche Scientifique FNRS Communauté française de Belgique through the funding of a FRIA grant under grant number 40021962.

Disclosure of Interests. The authors declare that they have no known competing financial interests or personal relationships that could have appeared to influence the work reported in this paper. The third author gratefully acknowledges the support of the Fonds de la Recherche Scientifique FNRS Communaut franaise de Belgique through the funding of a Postdoctoral Researcher (CR) mandate under grant number 40010864, and the support of Innoviris under project reference 2023-RDIR-49

References

1. Senthivel, R., Lourenço, P.B.: Finite element modelling of deformation characteristics of historical stone masonry shear walls. Eng. Struct. **31**(9), 1930–1943 (2009)
2. Hermans, Y., Grillanda, N., Ehab Moustafa Kamel, K., Milani, G., Massart, T.J.: Efficient image-based homogenized limit analysis for irregular masonry with lumped mortar joints representation. Eng. Struct. **318**, 118688 (2024)
3. Hermans, Y., Ehab Moustafa Kamel, K., Debeir, O., Milani, G., Massart, T.J.: Image-based structural kinematic limit analysis for historical masonry structures. Meccanica **60**, 2107–2124 (2025)
4. D'Altri, A.M., et al.: Modeling strategies for the computational analysis of unreinforced masonry structures: review and classification. Arch. Comput. Meth. Eng. **27**, 1153–1185 (2020)
5. Lourenço, P.B., de Borst, R., Rots, J.G.: A plane stress softening plasticity model for orthotropic materials. Int. J. Numer. Meth. Eng. **40**, 4033–4057 (1997)
6. Gatta, C., Addessi, D.: Orthotropic multisurface model with damage for macromechanical analysis of masonry structures. Eur. J. Mech. A. Solids **102**, 105077 (2023)
7. Wang, Q., Dos Santos, K.R.M.., Beyer, K.: Micro modeling of irregular stone masonry walls using mathematical programming. In: Endo, Y., Hanazato, T. (eds.) Structural Analysis of Historical Constructions, SAHC 2023. RILEM Bookseries, vol. 46, pp. 591–602. Springer, Cham (2023). https://doi.org/10.1007/978-3-031-39450-8_49
8. Lotfi, H.R., Shing, P.B.: Interface model applied to fracture of masonry structures. J. Struct. Eng. **120**(1), 63–80 (1994)
9. Alfano, G., Sacco, E.: Combining interface damage and friction in a cohesive-zone model. Int. J. Numer. Meth. Eng. **68**, 542–582 (2006)
10. Portioli, F., Casapulla, C., Gilbert, M., Cascini, L.: Limit analysis of 3D masonry block structures with non-associative frictional joints using cone programming. Comput. Struct. **143**, 108–121 (2014)
11. de Buhan, P., de Felice, G.: A homogenization approach to the ultimate strength of brick masonry. J. Mech. Phys. Solids **45**(7), 1085–1104 (1997)

12. Sacco, E.: A nonlinear homogenization procedure for periodic masonry. Eur. J. Mech. A. Solids **28**(2), 209–222 (2009)
13. Sonon, B., François, B., Massart, T.J.: A unified level set based methodology for fast generation of complex microstructural multi-phase RVEs. Comput. Meth. Appl. Mech. Eng. **30**(1), 116–136 (2012)
14. Kamel, K.E.M., Massart, T.J.: Towards automated image-based cohesive zone modeling of cracking in irregular masonry. Math. Mech. Solids **30**(1), 116–136 (2024)
15. Gilbert, M., Casapulla, C., Ahmed, H.M.: Limit analysis of masonry block structures with non-associative frictional joints using linear programming. Comput. Struct. **84**(13–14), 873–887 (2006)
16. Hua, Y., Milani, G.: New deformable element with arbitrary polygon shape for continuous modeling of limit analysis. Int. J. Solids Struct. **326**, 113745 (2026)
17. Simo, J.C.: Numerical analysis and simulation of plasticity. In: Handbook of Numerical Analysis, vol. 6, pp. 183–499 (1998)
18. Tiberti, S., Milani, G.: 2D pixel homogenized limit analysis of non-periodic masonry walls. Comput. Struct. **219**, 16–57 (2019)
19. Ministero delle Infrastrutture e dei Trasporti: Istruzioni per l'applicazione dell'aggiornamento delle Norme Tecniche per le Costruzioni di cui al Decreto Ministeriale 17 gennaio 2018. Gazzetta Ufficiale della Repubblica Italiana (2019)
20. Maier, G., Nappi, A.: A theory of no-tension discretized structural systems. Eng. Struct. **12**, 227–5234 (1990)
21. Milani, G., Lourenço, P.B., Tralli, A.: Homogenised limit analysis of masonry walls, part I: failure surfaces. Comput. Struct. **84**(3–4), 166–180 (2006)
22. Mascolo, I., Gesualdo, A., Olivieri, C., Fortunato, A.: On blocks detection in unilateral masonry-like structures: a rigid-elastic displacement approach. Int. J. Masonry Res. Innov. **7**(4), 395–405 (2022)
23. Olivieri, C., Cocking, S., Fabbrocino, F., Iannuzzo, A., Placidi, L., Adriaenssens, S.: Seismic capacity of purely compressed shells based on airy stress function. Continuum Mech. Thermodyn. **37**(2), 21 (2025)
24. Iannuzzo, A., Van Mele, T., Block, P.: Piecewise rigid displacement (PRD) method: a limit analysis-based approach to detect mechanisms and internal forces through two dual energy criteria. Mech. Res. Commun. **107**, 103557 (2020)
25. Iannuzzo, A., Montanino, A.: A limit analysis-based CASS approach for the in-plane seismic capacity of masonry façades. Int. J. Solids Struct. **289**, 112633 (2024)
26. Sangirardi, M., Di Santo, G., Amorosi, A.: An enriched and phenomenologically sound multilaminate model for masonry: JMM-E. Eng. Struct. **352**, 122113 (2026)